232 (2024) 212423

Contents lists available at ScienceDirect

Geoenergy Science and Engineering

journal homepage: www.sciencedirect.com/journal/geoenergy-science-and-engineering

Whirling dynamics of a drill-string with fluid–structure interaction

L.P. Volpi [a,b,*], E. Cayeux [b], R.W. Time [a]

[a] Universitetet i Stavanger, Kjell Arholms gate 41, Stavanger, 4021, Norway
[b] Norwegian Research Centre, Professor Olav Hanssens vei 15, Stavanger, 4021, Norway

ARTICLE INFO

Keywords:
Lattice-Boltzmann
Finite element
Fluid–structure interaction

ABSTRACT

Fluid–structure interaction models for drill-string vibrations are often of reduced order. However, both the structure and the surrounding fluid are non-linear, which can lead to complex coupled dynamic. In this paper, a coupled fluid–structure model is developed, where the flow is reduced to multiple cross-sections and solved with the lattice-Boltzmann method, while the finite element method is employed to discretize a region of the drill-string. In sequence, the whirling dynamics and the fluid forces are analysed for different configurations. The process is repeated disregarding the fluid-interaction with the aim of evaluating the fluid forces. The fluid forces estimated through the solution of the Navier–Stokes equation shows that the fluid acts in both dissipation and excitation of the vibrations. The dissipation is seen when high frequency dynamics is expected, whereas the lower frequencies are excited.

1. Introduction

When drilling to produce hydrocarbon resources or to create a geothermal well, a drill-string is used to connect the drill-bit to the drilling rig. The drill-string is composed of hollow pipes that allows to pump drilling fluids in the inside and to transport formation cuttings on the outside, in the space between the drill-string and the borehole, also referred as the annulus. The drill-string axial position is controlled by the hoisting system of the drilling rig, while its rotation is typically ensured by a top-drive motor. The drilling fluid that is circulated during the drilling operation is formulated to have a non-Newtonian rheological behaviour, and more specifically is shear thinning, such that the pressure losses inside the drill-string are not too excessive in view of the small cross-sectional area of the interior of the string, and at the same time has a high apparent viscosity at low shear rates to facilitate the transport of cuttings in the large cross-sectional area corresponding to the annulus.

The drill-string is an extremely slender structure. Estimation of the forces involved on the operation is relevant to proper control the process as it provides a tool for diagnosing harmful phenomena. While drilling, the structure is prone to vibrations which often lead to contact or collision with neighbouring walls. These impacts can lead to high-frequency vibrations, such as the rolling of the string around the borehole – the backward whirl – or in the opposite direction, forward whirl with sliding. Torsional oscillations in the drill-string can also happen due to the slenderness, which is directly connected to efficiency loss. Simultaneously, drilling fluids are pumped through the structure to transport cuttings out of the borehole. Even though it is an extremely important activity for the drilling process, it not only creates complex interactions with the surrounding fluid, but also generates large pressure difference between the inner region of the drill-string and its surroundings.

There are several models for drill-string vibrations. Lumped parameter models, such as the one described by Jansen (1993), have been broadly adopted in the literature with different levels of complexity. Yigit and Christoforou (2000) explored a similar model considering coupled torsional–lateral vibrations to aid in the control of the drilling operation. In a similar fashion, Melakhessou et al. (2003) provided a lumped model for lateral–torsional, with the addition of a bending degree of freedom. This model captured chaotic behaviour, with strong bouncing of the drill-pipes. These reduced order models are not limited to lateral and torsional vibrations. In the last years, de Moraes and Savi (2019) used a similar approach to model lateral–torsional–axial vibrations in the drill-string. While these reduced order models can describe accurately some of the phenomena, it often over-simplifies lateral interactions (Germay et al., 2009). This commonly reduces the analysis to a reduced section of the problem unless several degrees of freedom are used, such as provided by Liu et al. (2014). An alternative is to use continuous approaches. Ghasemloonia et al. (2014) conducted a continuous analysis of a coupled lateral–axial section of the drill-string. In this case, strong interaction between axial forces and the vibration modes – and natural frequencies – can be observed. Another popular approach is the use of the Finite Element Method (FEM) to

* Corresponding author at: Universitetet i Stavanger, Kjell Arholms gate 41, Stavanger, 4021, Norway.
E-mail addresses: lucas.volpi@uis.no (L.P. Volpi), erca@norceresearch.no (E. Cayeux), rune.time@uis.no (R.W. Time).

https://doi.org/10.1016/j.geoen.2023.212423
Received 16 August 2023; Received in revised form 3 October 2023; Accepted 20 October 2023
Available online 29 October 2023

discretize the continuous system. Khulief et al. (2007) provided a nonlinear model for coupled vibrations. This model, while computationally expensive, could be reduced by a modal truncation method, which limits the size of the system. Ritto (2010) provided another FEM-based model, with the addition of fluid forces due to the flow both inside and outside the drill-string. By including both the inner flow and pressure, there was a change in the modal behaviour of the drill-string, similar to what was observed with the inclusion of axial forces. A similar approach was taken by Tran et al. (2019) to model directional drilling with non-Newtonian rheological properties for the fluid.

When the fluid is concerned, two models are recurrent. The model provided by Jansen (1993) uses the concept of fluid drag and added fluid mass. In practice, it yields a nonlinear damping in which the damping coefficient escalates with the magnitude of the translation velocity as well as a modification in the inertia of the flow. The model from Fritz (1970) was initially provided for rotors and ultimately borrowed for drill-string vibrations. It consists in a reduced order model considering the flow in an annulus. Whereas the formulation accounts for quite complex behaviour, it does not directly regard non-Newtonian rheological fluids.

Often, the fluid-interaction models for drill-string vibrations do not take into account the fluid dynamic surrounding the structure. Given that many coupled nonlinear effects – such as collision – interacts with the flow, the fluid dynamic is often a source of uncertainties. In order to account for these effects, other computational methods can be employed to model the fluid. While the Finite Volume and Finite Difference Methods are common options, having a moving boundary condition – and a deformable mesh – can deteriorate the accuracy of the analysis (Busch and Johansen, 2020). An alternative is the lattice-Boltzmann Method (LBM), as it enables straightforward implementation of complex, moving boundaries. This method is based on the mesoscopic theory of the flow, which can recover the Navier–Stokes equation. From the mesoscopic point of view, convoluted boundary conditions can be dealt with simple approaches, such as the reflection of incoming fluid particles as it reaches a solid wall. One major characteristic is that this method is intrinsically transient. This makes the LBM a strong candidate for transient problems with moving boundaries.

Methods such as the one developed by Ladd (1994) and Noble and Torczynski (1998) can be used to directly estimate the fluid forces at the interface, resorting to neither simplified forcing schemes nor direct integration of the shear-stress at the surface of the structure. A third method, which is not limited to the LBM, is the immersed boundary method (Peskin, 1972). The method developed by Ladd consists in an extension to the traditional bounce-back method, which is the simplest form of solid boundary condition in the LBM. The method provided by Noble considers a separate collision operator for the solid phase and an averaging scheme which defines both solid and fluid regions, as well as the transition between them. This implies a smooth transition to the solid phase, hence the method is often referred to as the Partially Saturated Method (PSM). The immersed boundary (IB) is achieved by treating the interface as external forces. The IB method actually defines a family of methods, each using different forcing schemes or sub-methods. While all methods are known to be accurate with the proper discretization (Rettinger and Rüde, 2017), the second method is stable and does not require additional procedures to guarantee mass conservation. The main downside is that all solid nodes must be solved, which increases the computational time considerably for high solid–fluid area ratios.

The aim of this work is to provide a coupled fluid–structure interaction model for a section of the drill-string. To achieve this, a region of the drill-string is discretized with the finite-element method and a cross-section of the fluid domain is solved in the centre of each element of the model in order to find a distributed force for the structure. In sequence, whirling behaviours are analysed with different work conditions, i.e.: axial loads and inner pressures. The analysis is repeated for similar configurations where the fluid is disregarded. This way, the impact of the fluid in the overall dynamics is evaluated.

2. Models and methods

In this section, the development of the model is presented, as well as the methods used to discretize it. In Fig. 1 a simplified description of the problem is shown. The drill-string is composed by drill-pipes that are joined together by the tool-joints while it is immersed in the drilling fluid. The whole system is confined inside the borehole, which causes an eccentric annular cross-section. At the same time, there is a flow inside the drill-pipes which often causes a large pressure difference between the inner section of the pipe and the flow outside.

In this work, the axial flow properties are tackled separately from the tangential flow and is treated directly in the structure (Ritto, 2010; Tran et al., 2019). This is hereby obtained by considering the virtual work of the pressure gradient and the flow which, in practise, modifies the stiffness of the drill-string, similar to an axial compression. The tangential flow is modelled through the Navier–Stokes equation and is coupled with both the lateral and torsional vibrations. Treating the lateral interaction separately is a common simplification (Leine et al., 2002; Khulief and Al-Sulaiman, 2009; Yigit and Christoforou, 2000). In this case, this enables the creation of a fluid cross-section in each degree of freedom, where the fluid is to be solved independently.

As the problem regards both solid and fluid dynamics, two frames of references are used. One in the Lagrangian reference is defined by the Cartesian coordinate system with x, y and z and a second framework, which is Eulerian, is defined by X, Y and Z. Relevant values are shown in Appendix D and a list with the nomenclature can be found at the end.

2.1. Tool-joint vibration model

The drill-pipes are thinner and much longer than the tool-joints. Due to the larger radius, most of the impact and damage is expected at the tool-joints, which causes unbalances. Thus, the model assumes that the drill-pipes are slender and flexible, while the tool-joints are rigid and the only source of imbalance in the model. This eccentricity is considered to be aligned between tool-joints, as it is reasonable to assume that they come from abrasion. The drill-pipes are considered to be 9.7 m long, where 1.0 m corresponds to the tool-joint, this is repeated for a section of approximately 100 m of the drill-string. The extremities of the section are considered to be pinned, as it was observed in wells with large borehole irregularities. This lead to the isolation of the lateral vibrations of sections of the drill-string (Cayeux et al., 2018).

In Fig. 2, a schematic of the simplified model is presented, as well as the system of coordinates. The model includes lateral bending and torsion in the main axis, totalling 5 degrees of freedom ($\hat{\mathbf{q}} = \{u_x,\ u_y,\ \varphi_x,\ \varphi_y,\ \varphi_z\}^T$). Even though the cross-section is symmetric, the mass is considered to be off-centred by an arbitrary distance $\mathbf{e}(z,t)$ of the neutral line (Nelson and McVaugh, 1976).

Through the same figure, the relations between the undeformed and deformed cross-sections can be explicited. In the main axis, z, the displacement of a cross-section can be written according to the Euler–Bernoulli beam relations (Khulief et al., 2007):

$$\begin{cases} u_i = u_x + y(\cos\varphi_z - 1) + x\sin\varphi_z \\ u_j = u_y + x(\cos\varphi_z - 1) + y\sin\varphi_z \\ u_k = xu'_y - yu'_x, \end{cases} \tag{1}$$

where $\mathbf{u} = \{u_i, u_j, u_k\}^T$ are the displacements in the i, j and k directions in the global frame of reference, and $u' = \frac{\partial u}{\partial z}$.

With the Hamilton's principle, the weak form of the problem can be estimated as:

$$\int_0^{t_f} \mathcal{H}\, dt = \int_0^{t_f} (\delta K - \delta U + \delta W + \delta Q) dt = 0, \tag{2}$$

where δ is the variational operator and, K and U are the kinetic and potential energy, the work is represented by W and the energy exchanged at the inlet–outlet is Q.

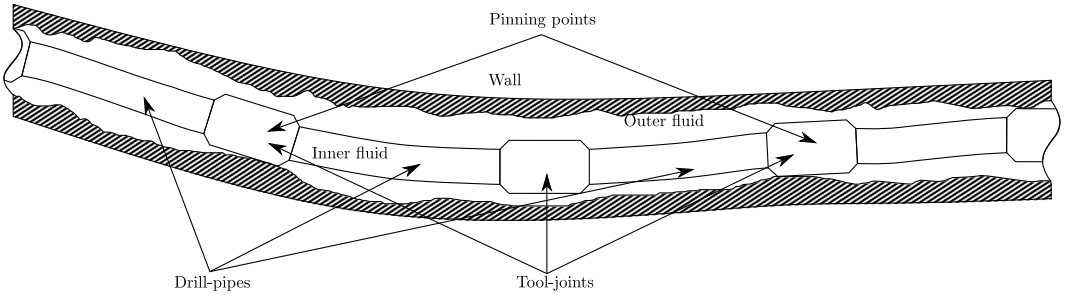

Fig. 1. Schematic of the drill-string and fluid problem.

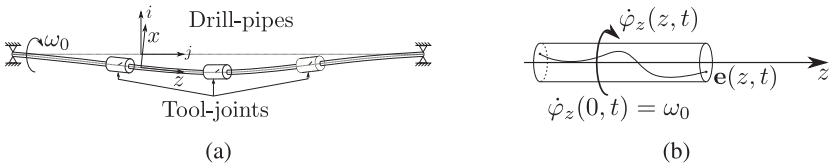

Fig. 2. Schematic of the continuous model for the structure. In (a) there is the tool-joint and the boundary conditions and in (b) the torsional degree of freedom and an arbitrary the eccentricity in mass.

The potential energy can be expressed as:

$$U = \frac{1}{2}\int_{\mathcal{V}} [E\epsilon_{zz}^2 + 4G(\gamma_{xz}+\gamma_{yz}) + \rho_s \mathbf{g}\cdot\mathbf{u}]d\mathcal{V}, \tag{3}$$

here, $\epsilon_{zz}^2 = u_k' + u_k'(u_i'^2 + u_j'^2 + u_k'^2) + \Delta(\theta^3)$, and only the shown nonlinear term is used as to acknowledge the large axial forces which are known to affect the lateral stiffness (Ghasemloonia et al., 2014; Khulief et al., 2007; Tran et al., 2019). The gravitational acceleration is $\mathbf{g}$.

For the kinetic energy, the mass is considered concentrated in a distance from the neutral line $\dot{\mathbf{d}} = \dot{\mathbf{u}}(0,0,z) + \dot{\mathbf{e}}(0,0,z)$, thus:

$$K = \frac{1}{2}\int_{\mathcal{V}} \rho_s \dot{\mathbf{d}}\cdot\dot{\mathbf{d}}\, d\mathcal{V} + \frac{1}{2}\int_L \rho_s \boldsymbol{\omega}^T \mathbf{I}\boldsymbol{\omega} dz + \frac{1}{2}\int_{\mathcal{V}_f} \rho_f \dot{\mathbf{u}}\cdot\dot{\mathbf{u}}\, d\mathcal{V} \tag{4}$$

where ρ_s and ρ_f are the densities of the structure and fluid,

$$\mathbf{e} = \{e_x, e_y, 0\}^T = |\mathbf{e}|(z)\{\cos\varphi_z,\ \sin\varphi_z,\ 0\}^T \tag{5}$$

is the position of the imbalanced concentrated mass of the tool-joints, with $\mathbf{e}(z)$ being the imbalance vector. This value is constant at the tool-joint and zero at drill-pipe regions, enforcing the aligned imbalance. The Young modulus, E, comes from the isotropic linear-elastic assumption. The vector $\boldsymbol{\omega}$ is the angular velocity in the global system of coordinates (Khulief et al., 2007; Ritto, 2010).

The terms regarding the fluid be defined as the energy exchanged at the inlets and outlets, which is expressed as a function of velocity inside the pipe $\mathbf{V}_{in}$ (Paidoussis, 1998; Ritto, 2010; Tran et al., 2019):

$$\delta Q = \int_S [(\dot{\mathbf{u}} + \mathbf{V}_{in})\cdot\delta\dot{\mathbf{u}}]\,\mathbf{V}_{in}\cdot d\boldsymbol{S}, \tag{6}$$

and the work due to pressure:

$$\delta W = \int_S \Delta P\cdot(\delta\mathbf{u}\cdot d\boldsymbol{S}). \tag{7}$$

Expanding the Hamiltonian, $\mathcal{H}$, and manipulating the derivatives, it can be rewritten as:

$$\begin{aligned}&\int_0^{t_f}\int_{L_s}[EI(\delta u_x''\, u_x'' + \delta u_y''\, u_y'') + GJ\delta\varphi_z''\varphi_z'' \\ &+(A_f\Delta P + \rho_s A_f V_{in}^2 + F_a)(\delta u_x'\, u_x' + \delta u_y'\, u_y') \\ &+(\rho_s A_s + \rho_f A_f)(\delta u_x\{\ddot{u}_x + g_x\} + \delta u_y\{\ddot{u}_y + g_y\}) + \rho_s J\delta\varphi_z\ddot{\varphi}_z \\ &-\rho_s A_s\dot{\varphi}_z^2(\delta u_x\, e_x + \delta u_y\, e_y)]dz\, dt = 0,\end{aligned} \tag{8}$$

where I is the area inertia and A_s is the area of the cross-section and A_f is the inner-fluid area. For this case, the geometrical non-linearities were disregarded, such as gyroscopic terms and inertial terms. Here, the term ΔP represents the difference in pressure between the inside and the outside of the pipe, and F_a is the resulting axial force in the section. The fluid is considered to be steady, removing transient terms in regard of ΔP and $\mathbf{V}_{in}$.

In this weak form, Finite Element Method (FEM) can be used to approximate the solution in of the equations of motion in terms of z, hence, it is assumed that $\hat{q}_l = \sum \mathbf{N}_l^T(z)\mathbf{q}_l(t)$ and $\delta\hat{q}_l = \sum \delta\mathbf{q}_l(t)^T\mathbf{N}_l(z)$, where $\mathbf{N}_l$ describes a family of shape function that follows Hermite polynomials used to discretize space, $\hat{\mathbf{q}}(z,t)$ is a generalized displacement vector containing the 5 degrees of freedom, and $\mathbf{q}(t)$ is the discrete version thereof.

This yields a global system of the form:

$$\mathbf{M}\ddot{\mathbf{q}} + (\mathbf{K} + \mathbf{K}_F)\mathbf{q} = \mathbf{F}_\mathbf{g} + \mathbf{F}_\mathbf{e}, \tag{9}$$

composed by the generalized inertia matrix, two stiffness matrices, the gravitational force vector and the imbalance force. At the neutral line, $\mathbf{u}$ becomes a subset of $\hat{\mathbf{q}}$ thus from here onward, $\mathbf{u}$ will be used when referencing to lateral displacements, and any angle will be made explicit.

The first stiffness matrix is due to the elasticity of the material, while the second is due to the combination of inner pressure, axial forces and inner flow. In this case, the effects of both pressure and axial force can be condensed into a single variable $F_k = (A_f\Delta P + F_a + \rho_f A_f V_{in}^2)$. These terms will be hereby explored as different combinations of force and pressure.

In addition, impact forces are considered if a section of the drill-string collides with the wall. In the direction normal to the contact, the force is assumed to be elastic during the collision:

$$\mathbf{F}_l^{(n)} = -H(r_l - \Delta r_{gap})[k_w(r_l - \Delta r_{gap}) + c_w\dot{\mathbf{u}}\cdot\boldsymbol{n}]\boldsymbol{n} \tag{10}$$

where r_l is the lateral displacement in the lth node, and ΔR is the contact gap. $H(r_l - \Delta R)$ is the step function, the constant k_w is the wall stiffness and is chosen as to emulate a no-displacement boundary condition at the wall. c_w is a wall damping that arises from a partially elastic impact.

The unit vector $\mathbf{n}$ points towards the contact direction. The tangential force follows the Coulomb's friction:

$$\mathbf{F}_l^{(t)} = \begin{cases} -(\sum \boldsymbol{F}\cdot\mathbf{t})\mathbf{t}, \text{ if } |\sum \mathbf{F}\cdot\mathbf{t}| \le \mu_s|\mathbf{F}_l^{(n)}| \\ -\mu_k|\mathbf{F}_l^{(n)}|\mathbf{t}, \text{ otherwise} \end{cases} \tag{11}$$

where μ_s and μ_k are the static and kinetic friction coefficients, and $\mathbf{t}$ is the unit vector in the direction tangential to the contact, pointing

towards the tangential velocity. The torque is calculated at the contact point as $\mathbf{T} = R\,(\boldsymbol{n} \times F_l^{(t)})$.

The final forces added to the system are the fluid forces. At first, a buoyancy force is added, and distributed, along the system. This model only consider the displaced fluid mass, and can be directly inserted in the body force by subtracting from the linear density term ($\rho_s A_s + \rho_f A_f$) the displaced fluid ($(A_s + A_f)\rho_f$).

In sequence, other fluid forces are estimated at the centre of the elements by solving the Navier–Stokes equation of the corresponding cross-section. Thus, it is expressed as:

$$\mathbf{F}_{\mathbf{f}_l} = \partial_z F_{lb_l}^{(x)} \mathbf{F}_{\mathbf{f}}^{(\mathbf{x})}{}_l + \partial_z F_{lb_l}^{(y)} \mathbf{F}_{\mathbf{f}}^{(\mathbf{y})}{}_l, \tag{12}$$

where $\mathbf{F}_{\mathbf{f}}^{(\mathbf{x})}{}_l$ and $\mathbf{F}_{\mathbf{f}}^{(\mathbf{y})}{}_l$ are obtained considering a uniform distribution of the force throughout each element while discretizing with the FEM, and $\partial_z F_{lb}^{(x)}$ and $\partial_z F_{lb}^{(y)}$ are the components of the force distribution estimated at each cross-section through the lattice-Boltzmann method. All of the lateral dissipation is assumed to be from the fluid forces. To obtain Eq. (12), it is necessary to calculate the forces in the middle of the element and then create the global forcing $\mathbf{F}_{\mathbf{f}_l}$. The torsional degrees of freedom assumed a Rayleigh proportional damping instead of fluid torques:

$$\mathbf{C}_{\varphi_z} = 10^{-4}\mathbf{M}_{\varphi_z} + 10^{-6}\mathbf{K}_{\varphi_z}. \tag{13}$$

In order to limit the presence of high-frequencies, a modal truncation is applied to the model, where only the eigenmodes associated with eigenfrequencies close to or lower than the excitation frequency are used during the numerical integration (Khulief et al., 2007). This is achieved by calculating the forces in the physical domain and transforming it to the modal base using only the eigenvectors associated with the desired eigenfrequency range.

Both extremities of the structure are considered pinned, while a constant rotation is prescribed at the top. Whereas this last condition can be set as an external force, care must be taken to assure that the torsional rigid body mode is present in the system when transforming to the modal base.

2.2. Fluid field model

The fluid fields are limited to the lateral cross-sections at the centre of each element. Here, it is assumed that most of the flow is lateral and any axial component is disregarded. In Fig. 3, both Eulerian and Lagrangian descriptions are presented, the former contains the fluid field and boundary conditions and the latter the kinematic of the geometric centre. The boundary conditions are dependent on the velocities of the inner and outer solid regions, $\mathcal{S}_i$ and $\mathcal{S}_o$. The velocity of the inner boundary depends directly on the velocity of the drill-string. While there is a bending of the drill-pipes, it is considered small and thus, the cross-section is assumed to be kept constant throughout the simulation. In order to solve the fluid dynamics, the lattice-Boltzmann method is used (LBM). This method is based on the discretization of the Boltzmann equation in space, time and velocity domains. It tracks the density distribution of the fluid, which can be used to recover macroscopic properties of the flow, such as pressure and velocity.

The density distribution defines the density of the flow in the control volume with velocity at a given direction. Briefly, the LBM consists in two main steps: (i) collision and (ii) propagation of the distribution. Outside the boundaries, both steps can be expressed by a single equation:

$$\mathbf{f}(\mathbf{X} + \boldsymbol{c}\Delta t, t + \Delta t) = \mathbf{f}(\mathbf{X}, t) + \boldsymbol{C}(\mathbf{X}, t), \tag{14}$$

where $\mathbf{f} = \{f_0, \ldots, f_\alpha, \ldots\}^T$ is the density distribution function in the direction α, $\mathbf{X}$ is the spatial position in a Eulerian framework, Δt is the time-step, $\boldsymbol{c} = \{\mathbf{c}_0, \ldots, \mathbf{c}_\alpha, \ldots\}$ is the lattice velocity set, containing vectors in the direction α. Finally, the term $\boldsymbol{C}(\mathbf{X}, t)$ is the collision operator. It is hereby divided into two operators, one for the fluid-covered region and another for the solid-covered area (Noble and Torczynski, 1998): $\boldsymbol{C} = \boldsymbol{C}^{(f)} + \boldsymbol{C}^{(s)}$. The first operator considers multiple relaxation times, and is described as (Lallemand and Luo, 2000):

$$\boldsymbol{C}^{(f)} = (1 - \epsilon)[\boldsymbol{\mathcal{M}}^{-1}\boldsymbol{\Lambda}(\eta)\boldsymbol{\mathcal{M}}\,(\mathbf{f}^{(e)}(\rho, \mathbf{V}) - \mathbf{f}(\mathbf{X}, t))], \tag{15}$$

where $\mathbf{f}^{(e)}$ is the equilibrium density distribution, the matrix $\boldsymbol{\mathcal{M}}$ transforms $\mathbf{f}$ to the momentum base ($\mathbf{m} = \boldsymbol{\mathcal{M}}\mathbf{f}$). $\boldsymbol{\Lambda}$ is a diagonal matrix which contains multiple relaxation parameters. The solid collision operator is defined as:

$$\boldsymbol{C}^{(s)} = \epsilon\,([\mathbf{f}^{(e)}(\rho, \mathbf{V}_{\mathcal{S}_i}) - \mathbf{f}(\mathbf{X}, t)] + \left[1 - \frac{\Delta t}{\tau(\eta)}\right][\mathbf{f}^{(e)}(\rho, \mathbf{V}) - \mathbf{f}(\mathbf{X}, t)]). \tag{16}$$

Here, a linear averaging parameter $\epsilon \in [0, 1]$ is used to weight between solid and fluid regions, i.e.: $\epsilon = 0$ for a fluid region and $\epsilon = 1$ for solid (Noble and Torczynski, 1998). τ is one of the relaxation parameters, which depends on the discretization of the system and the kinematic viscosity of the fluid (η). The term $\mathbf{V}_{\mathcal{S}_i}$ indicates the velocity in the region inside the contour $\mathcal{S}_i$, which is defined by:

$$\mathbf{V}_{\mathcal{S}_i} = \dot{\mathbf{u}} + (\mathbf{X}_{\mathcal{S}_i} - \mathbf{r}) \times \boldsymbol{\omega}. \tag{17}$$

Eq. (17) simply rewrites the cross-section velocity in a field.

The force distributions along the main axis can be calculated as a function of the solid collision operator (Noble and Torczynski, 1998):

$$\partial_z \mathbf{F}_{\mathbf{lb}} = -\frac{\Delta X^2}{\Delta t} \sum_{\mathbf{X}_{\mathcal{S}_i}} \epsilon(\mathbf{X}) \sum_\alpha \mathbf{c}_\alpha C_\alpha^{(s)}. \tag{18}$$

Other details for the method, such as estimation of macroscopic properties and choice of other relaxation parameters, are defined in Appendix A.

Regarding the fluid rheological behaviour, it is considered to be shear-thinning, and is modelled by the Quemada constitutive relation (Quemada, 1998):

$$\eta = \eta_\infty \left(\frac{1 + [\dot{\gamma}/\dot{\gamma}_c]^p}{\chi + [\dot{\gamma}/\dot{\gamma}_c]^p}\right)^2, \tag{19}$$

where η_∞, $\dot{\gamma}_c$, p and χ are model constants. One advantage of this model is that, while it can recover a power-law-like fluid, it does not require any regularization as it does not present a singularity point at $\dot{\gamma} = 0\ \forall\ \chi \neq 0$. The change in viscosity is interpreted as a change in one of the relaxation parameters of the problem.

Table 1
Choice of inner pressure and resulting axial force.

Case	ΔP [MPa]	F_a [kN]
1	0	0
2	5	0
3	5	20

3. Results

In this section, the results are presented. This section is organized into two different parts. For the first part, the batch of simulations concerns the fully coupled model, while the choice of pressure and axial force is shown in Table 1. In the second part, some of the simulations are repeated without the fluid forces, in other words, only the finite element model is used. In the uncoupled case, only one imbalance value was used. The solutions are obtained by asynchronous integration, where first one lattice-Boltzmann time-step is conducted and then several iterations of the FE model are executed by the adaptative Runge–Kutta–Fehlberg. Further details on the stability and the numerical convergence are presented in Appendix B whereas details in the numerical integration and coupling thereof are presented in Appendix C.

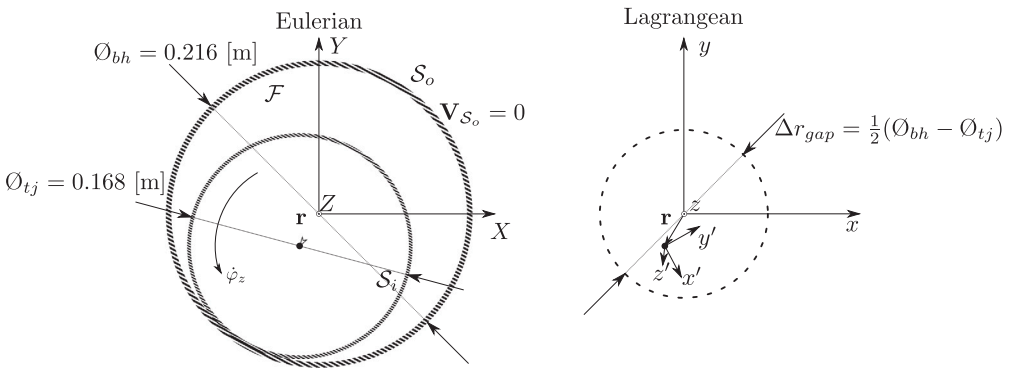

Fig. 3. Schematic of the cross-section with both Eulerian and Lagrangian descriptions.

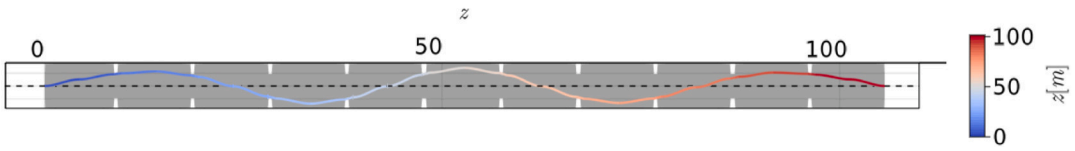

Fig. 4. Sample simulation with the displacement of the drill-string. The colour gradient refers to the position in z, and is a reference for future plots.

The impact model used for the structure expects some small overlap. This, however, can directly induce errors in the flow continuity, as the total solid area can decrease — in other words, the fluid area can increase. Hence the chosen contact gap is slightly smaller than the physical gap. In addition, the first 5 s of simulation are used to initialize the numerical integration, i.e.: the simulation would start with a developed tangential flow. In this step, the drill-string is only allowed to rotate. As there is no drill-string dynamic in this stage, the first 5 s are omitted from every result.

For the simulations, a grid with 160 × 160 cells was used for the fluid cross-section and the structure was divided into 42 elements, with 5 degrees of freedom each. Each tool-joint is discretized as 2 elements and the drill-pipes with 2 elements. The number of elements was defined by the numerical convergence of the natural frequencies under 40 rad/s of the stable configuration.

The modal truncation was applied to remove higher order natural frequencies (Khulief et al., 2007), and the criteria for truncation is that all natural frequencies under the excitation frequency must be present. The two extremities were considered pinned, and thus, their respective displacements were removed from the problem and the rotation at one of the end is prescribed as $\omega = 12.0$ rad/s, which is introduced in the model as an external force. The eccentric mass was considered to be equivalent at 1% of the tool-joint outer diameter, i.e.: $|\mathbf{e}| = 0.01R_{tj}$ A summary of other relevant values is presented in Appendix D.

Finally, every result here concerns the 6th tool-joint. This refers to the first tool-joint after the centre of the section. Some results will include the whole structure, and in those cases, it is stated explicitly.

To aid with the visualization, Fig. 4 is shown. It contains the solution of a simulation where the colour gradient refers to the position in z and, whereas it corresponds to a simulation, the Figure is distorted, as the high aspect-ratio of the model would compromise visualization. The dashed line is the centre of the borehole, while the grey surface represents the lateral gap for the respective section. The line with the colour gradient is the centre-line of the deformed drill-string, and is represented by the vector **u**. Note that, in this particular case, most tool-joints are in contact with the wall, whereas the drill-pipes are not. In addition, Fig. 5 shows another simulation case, where the use of the cross-sections can be exemplified.

3.1. Coupled model

In this subsection, the results are presented for the simulations with the fluid forces. In here, initially an imbalance of $|\mathbf{e}| = 0.01R_{o_{tj}}$ is used and a rotation of $\omega = 12$ rad/s. In this setup, six different drilling configurations are analysed — three vertical and three horizontal. In sequence, a critical scenario where the imbalance is $|\mathbf{e}| = 0.25R_{o_{tj}}$ is used. The orbits for the geometrical centre of the 6th tool-joint and the available gap are shown for each case in Fig. 6. Initially, a vertical section is considered, where both buoyancy and gravitational forces are incorporated in the resulting axial force (Figs. 6(a)–6(c)). The Figs. 6(d)–6(f) corresponds to the case where the section is perfectly horizontal and hence, the gravity and buoyancy are considered independently.

Fig. 7 shows the forces estimated for each dynamic. As seen in Figs. 6(d)–6(f), the results for the vertical case are similar with each other. This was repeated in relation to the results and, for this reason, only the first horizontal case ($F_a = 0$ N and $\Delta P = 0$ Pa) is presented. Note that Figs. 7(b) and 7(c), there is a high peak which is highlighted with a dashed line. This is connected to the collision of the tool-joint in question with the borehole, which translates into the fluid forces.

Fig. 8 presents the torsional velocities at the central tool-joint. Each plot includes a zoomed section to better describe the details of the vibration.

In Fig. 9, the whirl frequency is shown for the cases 1 and 2 in the vertical configuration. This was achieved by applying a fast Fourier transform to the complex representation of the radial displacement ($\hat{r} = u_x + iu_y$). In this figures, the average magnitude along the structure is presented, as well as the band defined by the maxima and minima. This transformation was applied to only those two cases as the other orbits in Fig. 6 presented simple dynamics.

Finally, the radial displacements of each node is displayed in Fig. 10. The colour gradient presents different positions along the drill-string, according to the colour gradient in Fig. 5. To better visualize, the tool-joint degrees of freedom are shown in a different section of the degrees of freedom of the drill-pipes, although both follow the same colour scale.

After this first set of results, the unbalance is increased to 25% of the outer tool-joint radius. If the maximum imbalance is in the magnitude of $|\mathbf{e}|_{max} = R_{o_{tj}} - R_{i_{tj}} \approx 42.7$ mm (Table D.1), this new unbalance is close to half this value $|\mathbf{e}| = 0.5|\mathbf{e}|_{max}$. This represents a severe case, where strong unbalance was present (Cayeux et al., 2018). With the new setup, only the vertical cases were simulated with the last two configuration of axial force and pressure difference. This is presented as those were considered the most critical cases. In Fig. 11 shows the orbits of the 6th tool-joint in this new scenario.

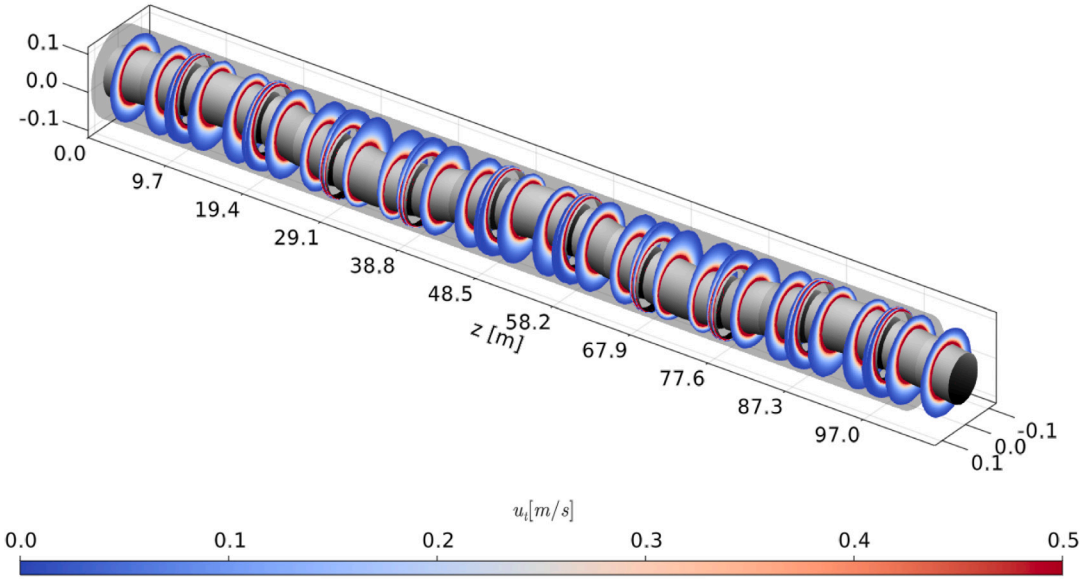

Fig. 5. Sample simulation with the displacement of the drill-string with cross-sections.

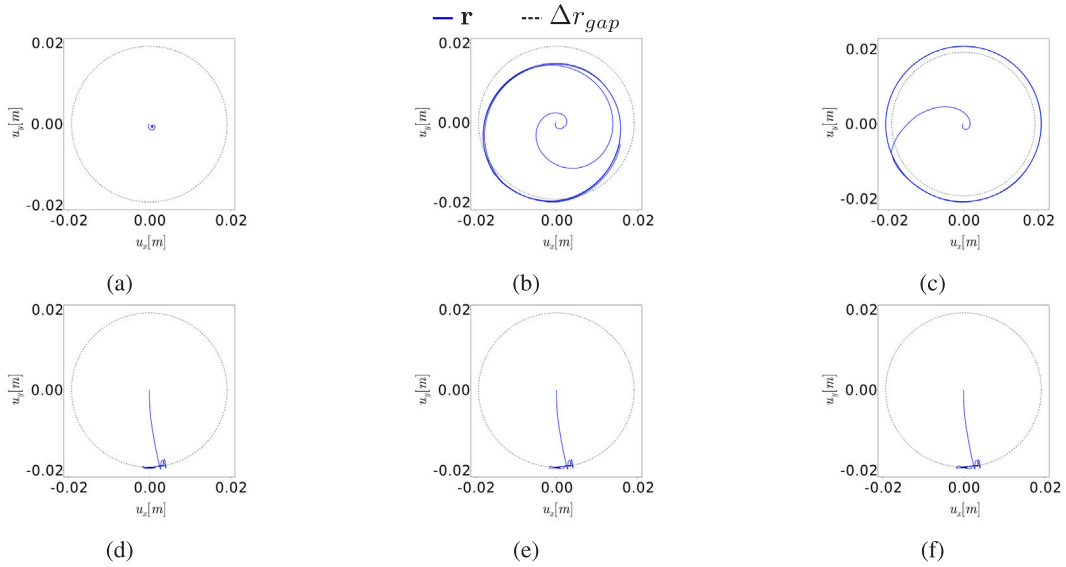

Fig. 6. Calculated orbits of geometric centre of the 6th tool-joint (a) case 1 in a vertical section, (b) case 2 in a vertical section, (c) case 3 in a vertical section, (d) case 1 in a horizontal section, (e) case 2 in a horizontal section and (f) case 3 in a horizontal section.

Following a similar fashion, the forces are shown for each case in Fig. 12 and the radial displacements are presented in Fig. 13.

3.2. Uncoupled model

In this subsection, the analyses are repeated without hydraulic calculations. The results are presented in a similar fashion, with the orbits, torsional velocities and radial displacements. As the Navier–Stokes equation was not solved, no fluid forces are calculated in this part. Only the cases with smaller imbalance are present here, with the force/pressure configurations from Table 1.

In Fig. 14 the orbits of the six cases are presented. The initial conditions were the same as in the previous simulations, with the centred positioning of the drill-string. In the sequence, Fig. 15 presents the torsional velocities of all cases without fluid.

The radial displacements of fluid-less case is shown in Fig. 15 . As before, the colour gradient refers to the position of the depicted node whereas black lines are reserved for tool-joints. Finally, the frequency domain analysis of the whirling is shown in Fig. 17 . Only cases 2 and 3 for the vertical setup are hereby presented as there is no evidence of other relevant whirling phenomenon in the other cases.

4. Discussion

In this section, the results presented are discussed. The objective of this study is to analyse the impact of hydraulic forces and torques on the dynamic mechanical deformations of a portion of drill-string. This is analysed by comparing Sections 3.1 and 3.2.

When the orbit of the vertical case, with neither axial forces nor axial flow, is compared with the fluid-less case, it is visible that the presence of fluid introduces vibrations, although of small intensity (Figs. 6(a) and 14(a)).

When pressure difference is introduced (Figs. 6(b) and 14(b)), it is observed that the fluid strongly reacts to the drill-string, retarding the initial impact with the borehole wall. By analysing the forcing terms in Fig. 7(b), a high-amplitude oscillation is present at a low

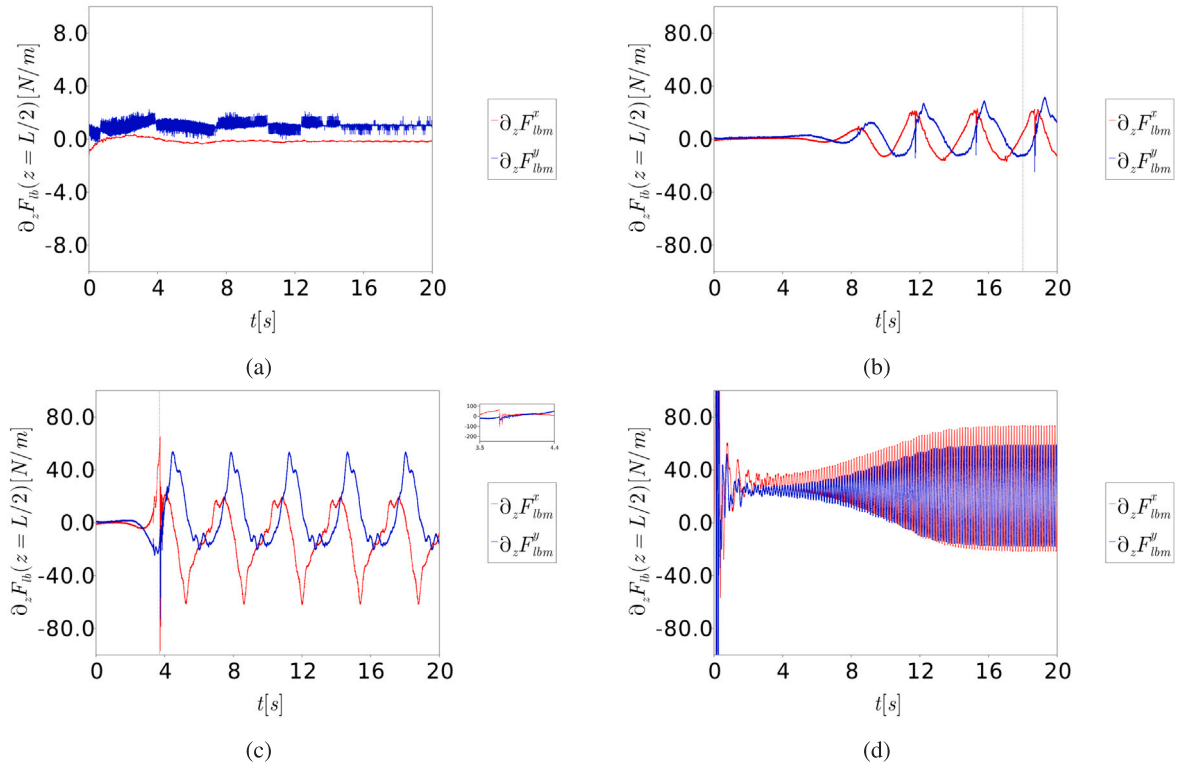

Fig. 7. Calculated forces on the 6th tool-joint (a) case 1 in a vertical section, (b) case 2 in a vertical section, (c) case 3 in a vertical section, and (d) case 1 in a horizontal section.

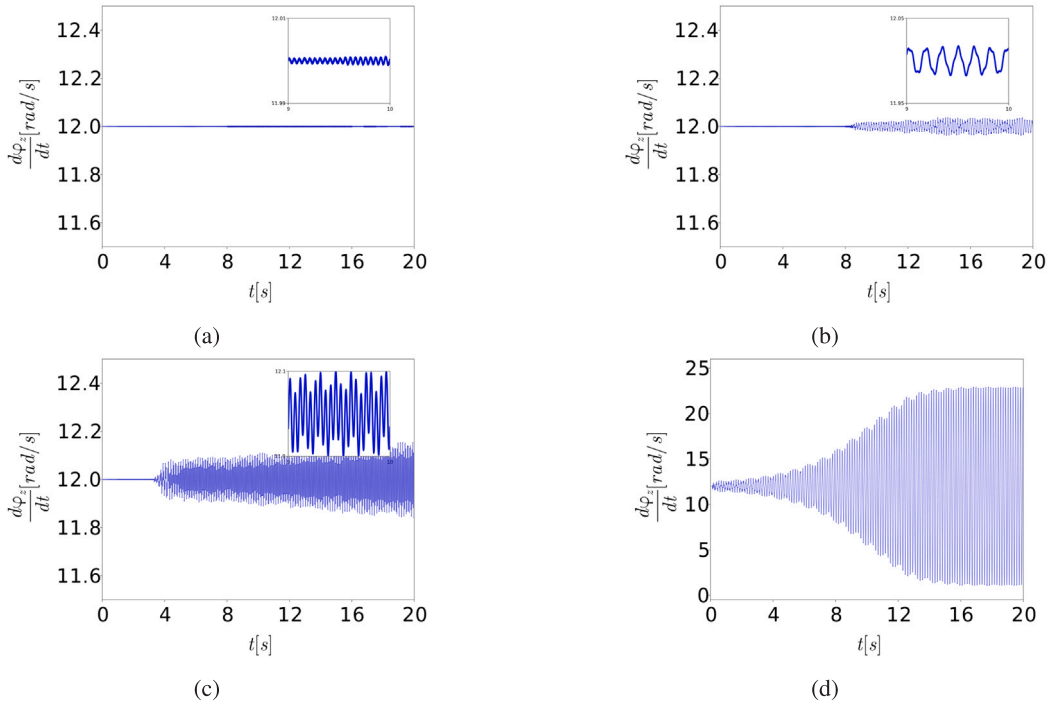

Fig. 8. Calculated torsional velocities $\dot{\varphi}_z$ of geometric centre of the 6th tool-joint (a) case 1 in a vertical section, (b) case 2 in a vertical section, (c) case 3 in a vertical section, (d) case 1 in a horizontal section.

frequency. This is an indication that, even at contact with the borehole, the drill-string is at a low-frequency regime. This is re-iterated by the whirling frequency shown in Fig. 9(a), which shows a low frequency asynchronous forward whirl. In contrast, Fig. 17(a) shows a predominant negative whirl frequency of higher magnitude. This indicates that the structure is mainly at a complex pattern of backward whirl. Thus, in contrast with the previous case, where the fluid was exciting the vibration, in this case the fluid is acting as a dissipative agent. From the radial displacements in Figs. 10(a) and 16(a), it is noticeable how the higher frequencies in displacement are damped. In addition, only

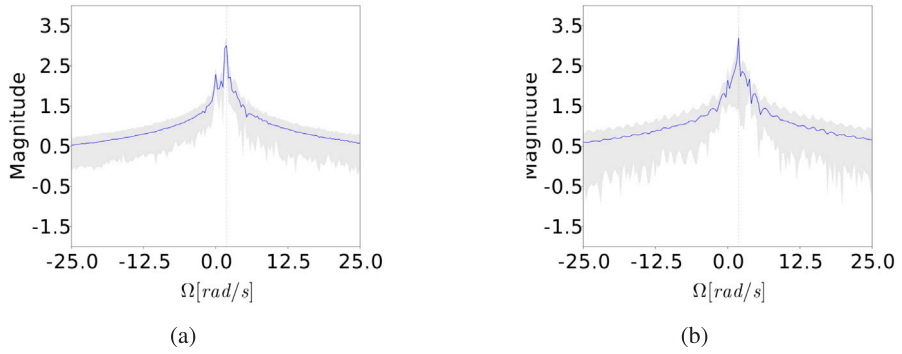

Fig. 9. Frequency domain analysis of $\hat{r} = u_x + iu_y$ for cases (a) 2 and (b) 3.

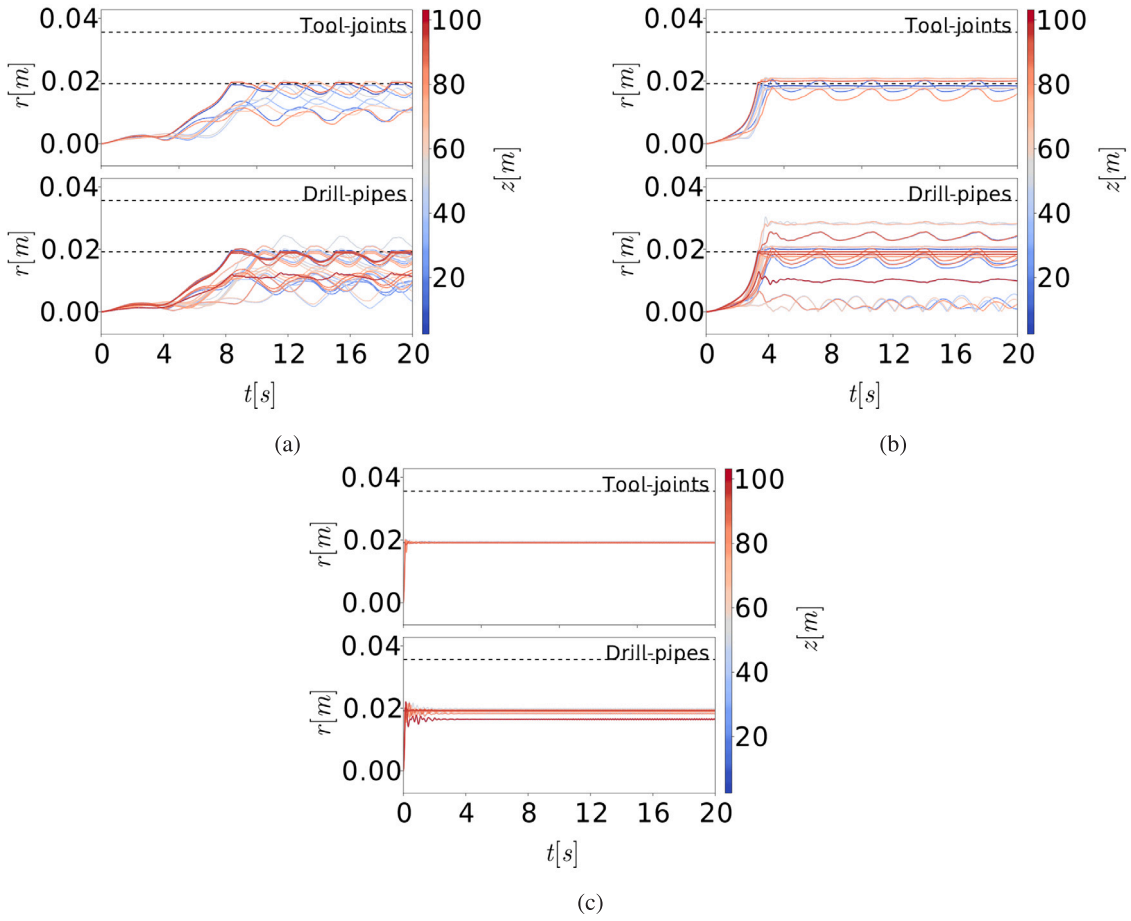

Fig. 10. Radial displacements along the drill-string. The colour scale represents the position and the dashed-line the available gap — one for the drill-pipes and the other at the tool-joint. The vertical cases are presented in: (a) for the second, and in (b) for the third. Likewise, the horizontal case is shown in (c).

the tool-joints collide with the wall when the fluid is present, whereas without fluid, sections of drill-pipes also collide with the wall. The occurrence of contact between pipe sections on the wall is extremely relevant, as collision and even permanent contact can be a source of damage through impact or even abrasion. At the same time, high-frequency vibrations are directly connected with the fatigue of the structure. When there is fluid, the drill-string has a larger overlap with the borehole. While this is a side effect of the numerical method used, it indicates that the flow dampens vibrations but also increases the forces in the radial direction — flow-induced vibrations.

Much of the tendencies are repeated as the axial force is added. In orbits (Figs. 6(c) 14(c)) show that the impact is delayed and the frequency domain in Figs. 9(b) and 9(b) once again show signs of different dynamics, where the fluid leads to a low-frequency vibration while the fluid-less case shows high-frequency backward whirl. When the drill-string collides with the wall, high peaks of fluid forces are observed (Figs. 7(c) and 7(c)). The magnitude is much higher than for the rest of the dynamic, with large fluctuations at a high frequency.

When the horizontal cases are analysed, it is observed that changes in axial flow and axial force do not impact greatly the dynamic. An analogy between Figs. 6(d)–6(f) and 14(d)–14(f) shows that the fluid forces displace the drill-string asymmetrically – a manifestation of the Magnus forces. At the same time, the fluid forces are extremely effective in mitigating high-frequency oscillations in the drill-string.

The presence of the Magnus effect is confirmed through the pressure and velocity gradients of the cross-section, shown in Fig. 18, as both

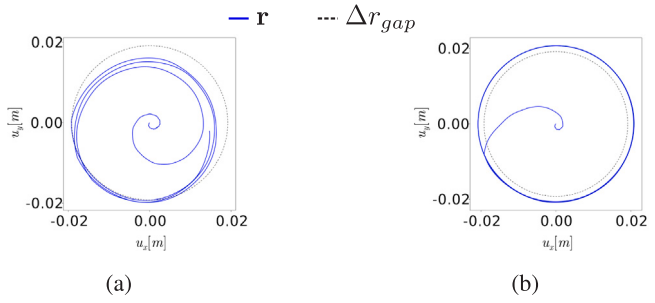

Fig. 11. Calculated orbits of geometric centre of the 6th tool-joint with the larger imbalance. In (a) is the case 2 in a vertical section, (b) the case 3 in a vertical section.

fields become asymmetric. Most fluid models, however, assumes that the fluid acts as a viscous damper. This type of interaction models is unable to capture the Magnus effect.

At the same time, through Fig. 8(d), it is observed that torsional vibration is introduced to when there is fluid. The communication between lateral and torsional degrees of freedom is solely done by the impact torques. This means that the balance between lateral fluid forces and the contact forces generates a high-frequency torque, which excites the drill-string. Due to the lack of strong dissipation, this vibration settles in a resonance-like behaviour, and thus, it is as the lateral forces are inducing torsional vibrations.

The increase of the unbalance did not change most of the dynamic. While qualitatively similar, the use of high pressures and high forces is impacting the most. In a unstable case, any imbalance creates a large disturbance in the model.

5. Concluding remarks

In this work, a fluid–structure interaction model for a drill-string is provided based on the coupled solution of both the drill-string vibration problem and the Navier–Stokes equation. The model provided is limited to lateral and torsional vibrations, whereas axial flow is assumed to interact to the structure independently of the lateral flow. For this, the Finite Element Method is used to discretize the structure while the Lattice-Boltzmann Method is used to solve the Navier–Stokes equation.

Six different configurations are analysed, with different drill-string orientations, axial flows and axial forces. In order to evaluate the effects of the fluid, all simulation were repeated without the fluid forces and the results were compared.

It is observed that the fluid, while acting as a dissipative agent, also generated vibrations. This effect is mostly noted in the torsional degrees of freedom, while not limited to those. The fluid damped out the vibrations with the exception of when low vibrations are expected. When there is a horizontal section, the combination of fluid lateral forces and contact forces acted as an excitation for the torsional degrees of freedom, creating a severe vibration case.

When there is an asymmetric dynamic, the Magnus effect is observed. This is relevant as this behaviour cannot be captured by simpler viscous damping models.

In summary, the coupled model shows that the fluid interaction leads to both dissipation and excitation of drill-string vibrations. The dissipative properties are mostly present at high-frequencies, whereas the excitation is in the lower frequency region. Whirl analyses in different scenarios also shows that the fluid has an important place in prevention of backward whirl.

Declaration of competing interest

The authors declare that they have no known competing financial interests or personal relationships that could have appeared to influence the work reported in this paper.

Data availability

Data will be made available on request.

Acknowledgements

This research was funded by the The Research Council of Norway, Equinor and Sekal.

Appendix A. Lattice-Boltzmann

A common two-dimensional lattice configuration is presented in Fig. 19, where there are 9 possible lattice velocities ($\mathbf{c}_\alpha$ with $\alpha \in [0, 8]$) represented by the 8 arrows and the 0 velocity at the centre and with square lattices.

The lattice-Boltzmann has as a main variable the density distribution with a given velocity. The density field, velocity field and shear-rate tensor can be recovered from the statistical moments:

$$\rho_f = \sum_\alpha f_\alpha, \qquad \rho_f \mathbf{V} = \sum_\alpha \mathbf{c}_\alpha f_\alpha, \tag{A.1}$$

and the rate-of-strain tensor (Chai et al., 2011):

$$\dot{\boldsymbol{\gamma}} = -\frac{1}{2\rho_f c_s^2} \sum_\alpha \mathbf{c}_\alpha \mathbf{c}_\alpha (\boldsymbol{\mathcal{M}}^{-1} \boldsymbol{\Lambda} \boldsymbol{\mathcal{M}})(f_\alpha - f_\alpha^{(e)}). \tag{A.2}$$

Those are used to calculate the equilibrium distribution:

$$f_\alpha^{(e)} = \rho_f w_\alpha \left[1 + \frac{\mathbf{V}\cdot\mathbf{c}_\alpha}{c_s^2}\left(1 + \frac{\mathbf{V}\cdot\mathbf{c}_\alpha}{2c_s^2}\right) - \frac{\mathbf{V}\cdot\mathbf{V}}{2c_s^2}\right], \tag{A.3}$$

where w_α is a weight constant and $c_s^2 = \frac{\Delta X^2}{3\Delta t^2}$ is the lattice sound speed. Both are dependent on the type of lattice used. In this particular case, the computations are directly conducted in the momentum base, $\mathbf{m}^{(e)} = \boldsymbol{\mathcal{M}}\mathbf{f}^{(e)}$, as this yields into simplifications in the operations. Matrix $\boldsymbol{\mathcal{M}}$ is orthonormal and is obtained by applying the Gram–Schmidt method into another matrix which defines the transformation to the momentum base. This method allows the use of a diagonal matrix $\boldsymbol{\Lambda}$ for the relaxation parameters.

The relaxation matrix $\boldsymbol{\Lambda} = \text{diag}(\{0,\ \omega_e,\ \omega_\epsilon,\ 0, \omega_e,\ \omega_q,\ 0,\ \omega_q,\ \omega_\eta,\ \omega_\eta\})$, where the choice of parameters ω_i directly affect the accuracy and stability of the model. The last parameter is directly related with the relaxation time $\omega_\eta = \frac{\Delta t}{\tau}$. The other parameters were varied and did not seem to greatly affect accuracy, with the exception of when close to $\omega_i \to 2$. For the sake of stability, they were chosen as $\omega_e = 1.1$, $\omega_\epsilon = 1.0$, and $\omega_q = 1.0$. This means that higher moments were fully – or close to – relaxed.

Finally, the kinematic viscosity is related to the relaxation parameter τ:

$$\eta = c_s^2(\tau - \Delta t/2). \tag{A.4}$$

As a non-Newtonian rheology is considered, the shear-rate dependency creates an implicit problem in Eqs. (A.2) and (A.4). A common way to simplify the problem is to consider the values estimated from the previous time step and simply recalculate τ and η to be used in the next iteration.

Finally, the method is usually regularized to obtain a dimensionless system where $\rho_f^* = 1$, $\Delta X^* = 1$ and $\Delta t^* = 1$. To do so, the conversion constants are set to:

$$C_{\Delta X} = \frac{\Delta X}{\Delta X^*}, \quad C_{\rho_f} = \frac{\rho_f}{\rho_f^*}, \text{ and } C_\eta = \frac{3\,\eta_{\min}}{(\tau^* - 1/2)}, \tag{A.5}$$

which yields a (physical) time-step of $\Delta t = C_{\Delta X}^2 / C_\eta$. With these conversion constants defined, all variables can be rewritten in the LBM units. The time conversion is dependent on the kinematic viscosity:

$$C_{\Delta t} = \frac{C_{\Delta X}^2}{C_\eta} \tag{A.6}$$

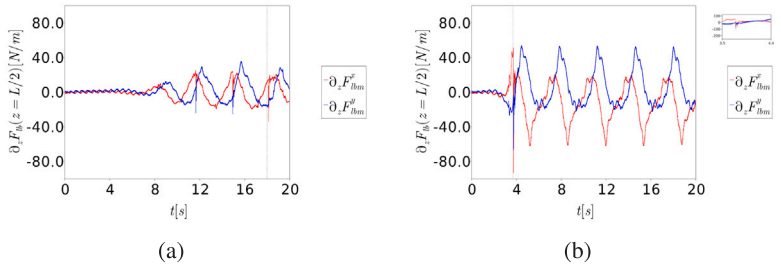

Fig. 12. Estimated forces orbits of the 6th tool-joint with the larger imbalance. In (a) is the case 2 in a vertical section, (b) the case 3 in a vertical section.

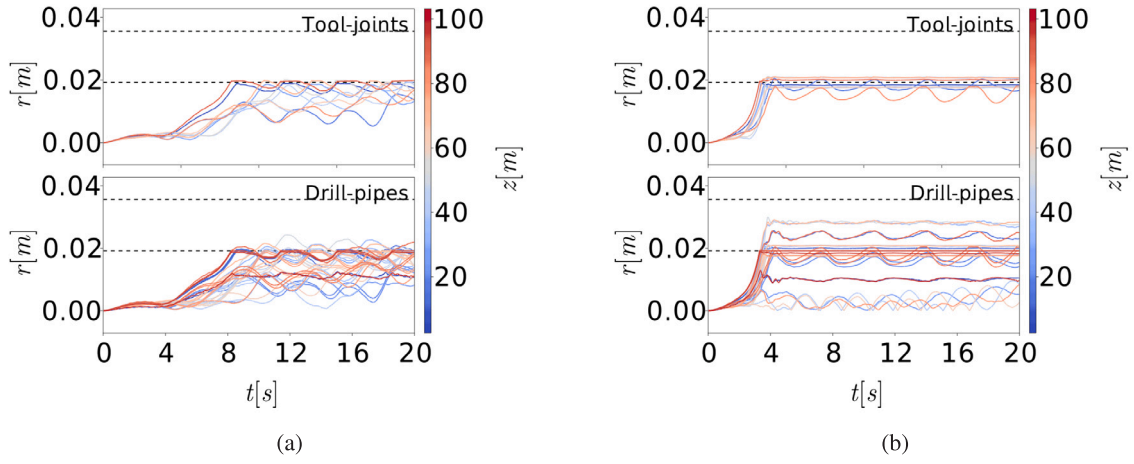

Fig. 13. Radial displacements along the drill-string with larger imbalance. The colour-scale represents the position and the dashed-line the available gap — one for the drill-pipes and the other at the tool-joint. The vertical cases are presented in: (a) for the second, and in (b) for the third.

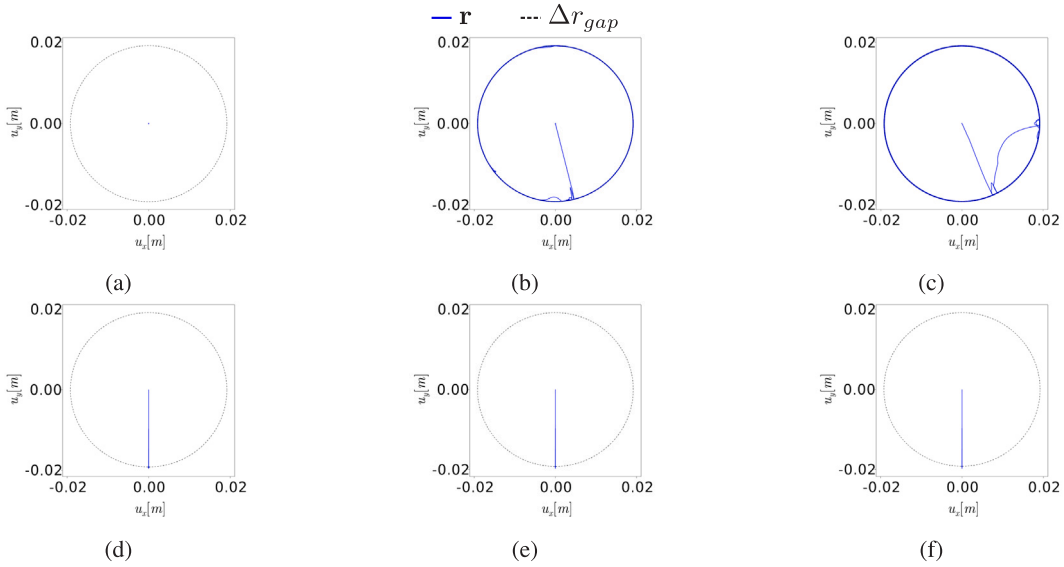

Fig. 14. Calculated orbits of geometric centre of the 6th tool-joint (a) case 1 in a vertical section, (b) case 2 in a vertical section, (c) case 3 in a vertical section, (d) case 1 in a horizontal section, (e) case 2 in a horizontal section and (f) case 3 in a horizontal section.

The remaining conversion parameters use combinations of these, e.g.:

$$C_V = \frac{C_{\Delta X}}{C_{\Delta t}}, \quad C_\Omega = \frac{1}{C_{\Delta t}}, \quad C_m = C_{\rho_f} C_{\Delta X}^3, \text{ and } C_F = \frac{C_m C_{\Delta X}}{C_{\Delta t}^2} \tag{A.7}$$

for the velocity, rotational speed, mass, and force, respectively. Before conducting the lattice-Boltzmann step, properties from the structure are converted with the parameters above. The displacement **u** is then divided by $C_{\Delta X}$, for example.

Appendix B. Stability and numerical convergence

The lattice-Boltzmann stability depends on the choice of relaxation parameter $\frac{\Delta t}{\tau}$ and the number of cells. As $\frac{\Delta t}{\tau} \to 1/2$, the method

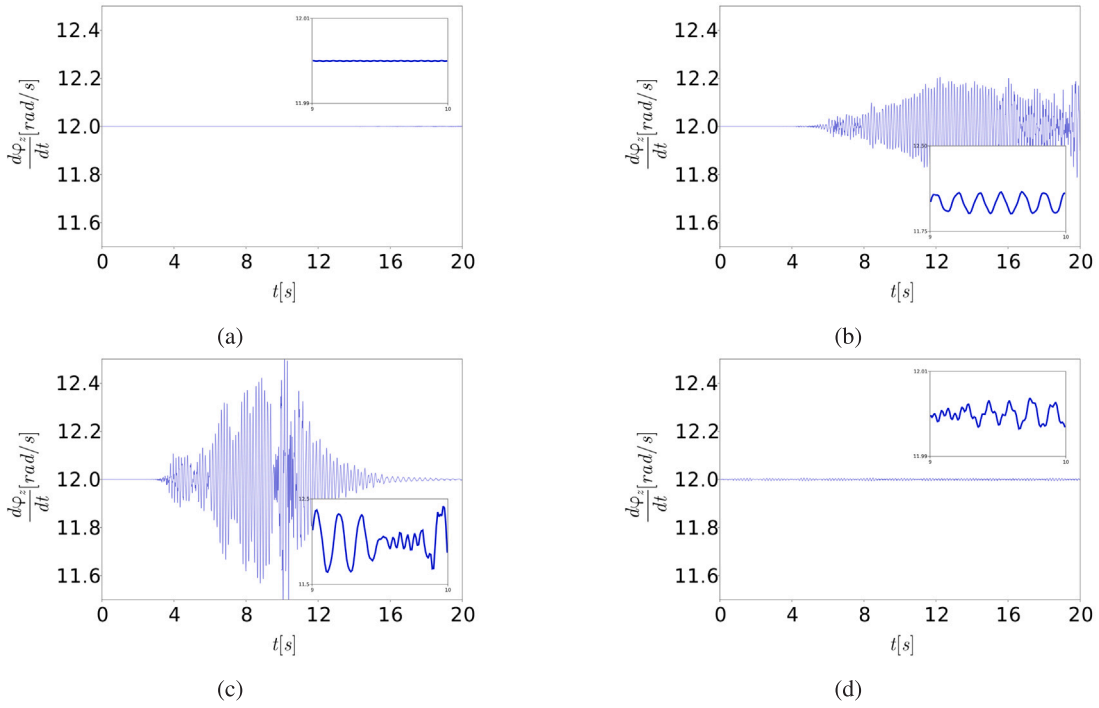

Fig. 15. Calculated torsional velocities $\dot{\varphi}_z$ of geometric centre of the 6th tool-joint (a) case 1 in a vertical section, (b) case 2 in a vertical section, (c) case 3 in a vertical section, (d) case 1 in a horizontal section.

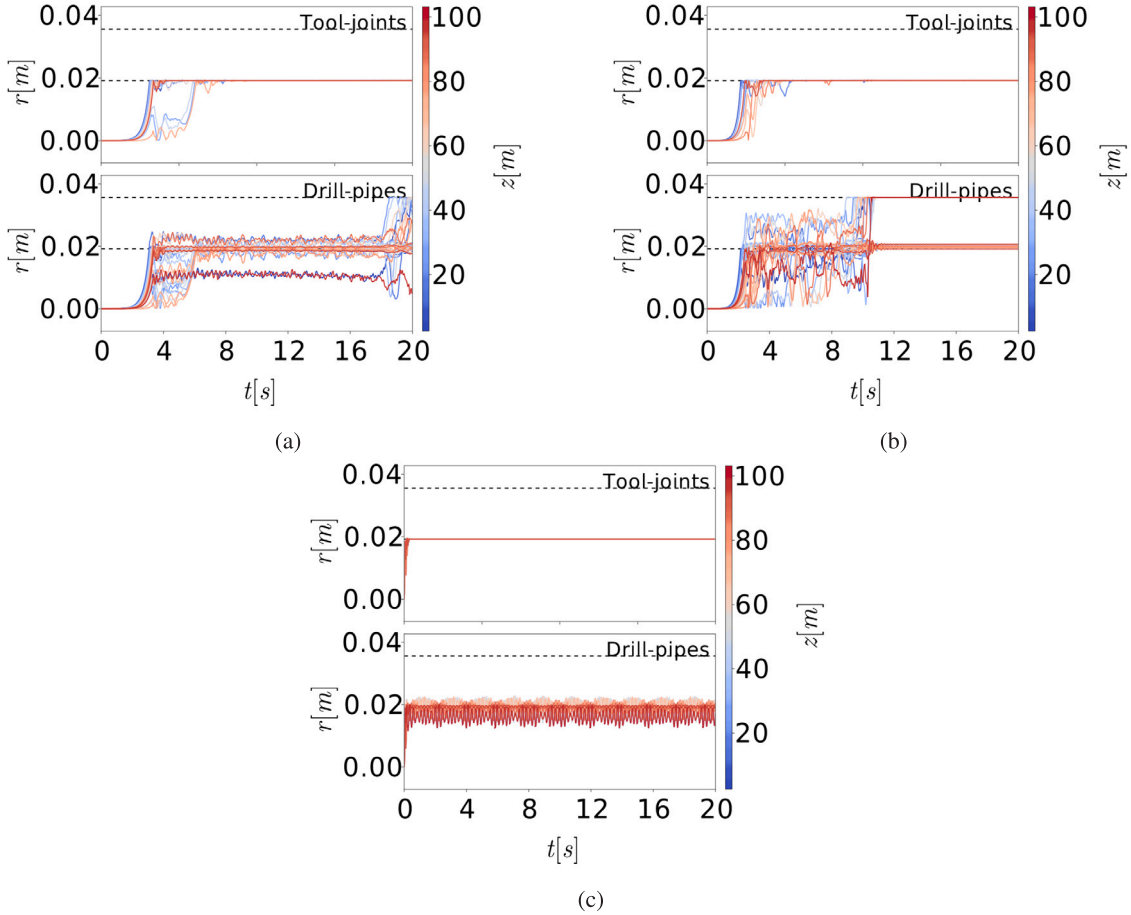

Fig. 16. Radial displacements along the drill-string. The colour-scale represents the position and the dashed-line the available gap — one for the drill-pipes and the other at the tool-joint. The vertical cases are presented in: (a) for the second, and in (b) for the third. Likewise, the horizontal case is shown in (c) for the first configuration.

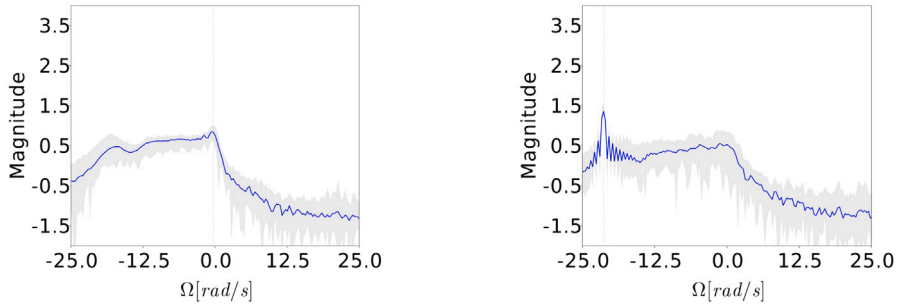

Fig. 17. Frequency domain analysis of $\hat{r} = u_x + iu_y$ for cases (a) 2 and (b) 3 without fluid forces.

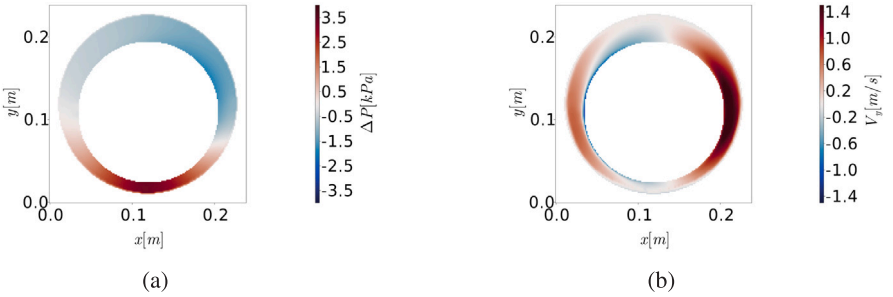

Fig. 18. Fluid fields at the 6th tool-joint for (a) pressure, (b) velocity in the y-direction.

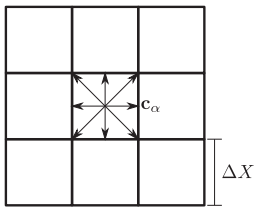

Fig. 19. Schematic of the lattice-Boltzmann discretization.

becomes unstable. The same is true if the flow velocity is large in comparison to the lattice sound speed (c_s), which leads to the compressibility of the flow. If all relaxation times are considered the same, i.e.: $\boldsymbol{\Lambda} = \frac{\Delta t}{\tau}\mathbf{I}$, the collision operator returns the single relaxation time, or the Bhatnagar–Gross–Krook (BGK) collision operator. However, using different relaxation times allows to relax non-hydrodynamic moments, which adds to the stability of the simulation, especially when $\frac{\Delta t}{\tau} \to 1/2$ (Dellar, 2003).

Given the stability constraints, the choice of time-step in the lattice-Boltzmann is limited. It is reasonable to assume that the characteristic times of the structure are smaller than those of the fluid, and thus, an explicit numerical integration would require smaller time-steps. To deal with this, both systems are integrated asynchronously and, in each LBM time-step, multiple time-steps are employed for the drill-string.

The convergence of the lattice-Boltzmann solver was analysed at a constant lattice velocity to guarantee that the flow velocity would be much smaller than the lattice sound speed ($|\mathbf{V}|_{\max} \ll c_s$). The lattice size ΔX and τ were adjusted until the desired accuracy.

The convergence for the structure regarded the convergence of the natural frequencies.

Appendix C. Numerical methods

As mentioned in Section 3, the numerical integration of the problem consists of two main, asynchronous, steps. The lattice-Boltzmann consists in two main steps, collision and propagation. For parallel implementation, the propagation is done in reverse, i.e.:

$$\mathbf{f}(\mathbf{X}, t) = \mathbf{f}^*(\mathbf{X} - \boldsymbol{c}\Delta t, t - \Delta t), \tag{C.8}$$

where $\mathbf{f}^*$ is the post-collision distribution. Two variables are used for $\mathbf{f}$, hereby defined as $f^{(1)}$ and $f^{(2)}$ to avoid rewriting a variable before it is worked at the proper time-step. Thus, it goes as:

(1) Start lattice-Boltzmann step at t with time-step Δt:

(I) Dispatch all LBM-related buffers to the acceleration unit (e.g.: GPU).

(II) Identify position (x, y) and use pre-collision distribution $f^{(1)}(x, y, l)$ for the following steps:

(A) Compute macroscopic fields from Eqs. (A.1) and (A.2).

(B) Convert $f_l(\mathbf{X} - c_l\Delta t, t - \Delta t)$ to the momentum base, using $\mathcal{M}\mathbf{f}$,

(C) Compute the equilibrium of the momentum ($m_l^{(e)}$), either by transforming $f_l^{(e)}$ or by estimating directly in the momentum base,

(D) Estimate local volume fraction ϵ using FEM displacements u_x and u_y. Those are interpolated at the centre of the element.

(E) Estimate local solid velocity field with Eq. (17).

(F) Collide using Eqs. (15) and (16).

(G) Mask fixed wall nodes and stream fluid nodes.

(H) Store new distributions at $f^{(2)}$

(III) Read buffers at the CPU level and synchronize domain.

(IV) Exchange pointers $f^{(1)} = f^{(2)}$.

Table D.1
Parametric information for the numerical simulations.

Name (symbol)	Value [unit]	Name (symbol)	Value [unit]
Drill-pipe outer radius	0.0635 [m]	Drill-pipe inner radius	0.0543 [m]
Tool-joint outer radius	0.0840 [m]	Tool-joint inner radius	0.0413 [m]
Borehole wall radius	0.108 [m]	Drill-string section length	105.7 [m]
Tool-joint length	2.0 [m]	Young's Modulus (E)	220.0 [GPa]
Poisson ratio (ν)	0.30	Solid density (ρ_s)	7800.0 [kg/m^3]
Kinetic friction (μ_k)	0.30	Static friction (μ_s)	0.60
Unbalance ($\|\mathbf{e}\|$)	8.40×10^{-5} [m]	Fluid density (ρ_f)	1101.0 [kg/m^3]
Infinity viscosity (η_∞)	2.36×10^{-2} [Pa s]	Characteristic shear-rate ($\dot{\gamma}_c$)	273.94 [1/s]
Quemada exponent (p)	0.436	–	–

(2) Start finite-element step at t with time-step $dt < \Delta t$:

(I) Calculate accelerations for both 4th and 5th order Runge–Kutta.

(II) Integrate for both 4th and 5th order Runge–Kutta.

(III) Evaluate convergence based on the solutions: $\|\mathbf{u}_{rk4} - \mathbf{u}_{rk5}\| <$ tolerance.

(A) If true:

(i) $t_{new} = t + dt$.

(a) Then, increase $dt_{new} \geq dt$

(b) Evaluate $t_{new} + dt_{new} > (t + \Delta t)_{lbm}$:

(1) If $t_{new} + dt_{new} > (t + \Delta t)_{lbm}$:

(I) correct dt_{new}, to $dt_{new} = (t+\Delta t)_{lbm} - t_{new}$.

(2) If $t_{new} + dt_{new} < (t + \Delta t)_{lbm}$:

(I) go to step 2.I using the value of t_{new} and new step dt_{new}.

(3) If $t = (t + \Delta t)_{lbm}$ is:

(I) True, return to step 1.

(II) False, go back to 2.I using $t = t_{new}$.

(B) If false:

(i) discard results, reduce ($dt_{new} < dt$) and re-start from 2.I at the old time-step t.

Appendix D. Geometry and parameters

In this appendix, values regarding the geometry and other parameters relevant to the simulation are summarized in Table D.1.

References

Busch, A., Johansen, S.T., 2020. Cuttings transport: On the effect of drill pipe rotation and lateral motion on the cuttings bed. J. Pet. Sci. Eng. 191 (June 2019), 107136. http://dx.doi.org/10.1016/j.petrol.2020.107136.

Cayeux, E., Skadsem, H.J., Carlsen, L.A., Stokland, L.M., Cruikshank, S., 2018. Analysis of asymmetric tool-joint wear while drilling long horizontal sections day 1 Wed, April 18, 2018. pp. D011S005R003, http://dx.doi.org/10.2118/191339-MS.

Chai, Z., Shi, B., Guo, Z., Rong, F., 2011. Multiple-relaxation-time lattice Boltzmann model for generalized Newtonian fluid flows. J. Non-Newton. Fluid Mech. 166 (5–6), 332–342. http://dx.doi.org/10.1016/j.jnnfm.2011.01.002.

de Moraes, L.P., Savi, M.A., 2019. Drill-string vibration analysis considering an axial-torsional-lateral nonsmooth model. J. Sound Vib. 438, 220–237. http://dx.doi.org/10.1016/j.jsv.2018.08.054.

Dellar, P.J., 2003. Incompressible limits of lattice Boltzmann equations using multiple relaxation times. J. Comput. Phys. 190, 351–370.

Fritz, R.J., 1970. The effects of an annular fluid on the vibrations of a long rotor, part 2—Test. J. Basic Eng. 92 (4), 930–937. http://dx.doi.org/10.1115/1.3425166, arXiv:https://asmedigitalcollection.asme.org/fluidsengineering/article-pdf/92/4/930/5639156/930_1.pdf.

Germay, C., Denoël, V., Detournay, E., 2009. Multiple mode analysis of the self-excited vibrations of rotary drilling systems. J. Sound Vib. 325 (1–2), 362–381. http://dx.doi.org/10.1016/j.jsv.2009.03.017.

Ghasemloonia, A., Geoff Rideout, D., Butt, S.D., 2014. Analysis of multi-mode nonlinear coupled axial-transverse drillstring vibration in vibration assisted rotary drilling. J. Pet. Sci. Eng. 116, 36–49. http://dx.doi.org/10.1016/j.petrol.2014.02.014.

Jansen, J.-D., 1993. Nonlinear dynamics of oil well drill strings. In: Proefschrift. Delft University, Stevinweg 1, 2628 CN Delft.

Khulief, Y.A., Al-Sulaiman, F.A., 2009. Laboratory investigation of drillstring vibrations. Proc. Inst. Mech. Eng. C 223 (10), 2249–2262. http://dx.doi.org/10.1243/09544062JMES1550.

Khulief, Y.A., Al-Sulaiman, F.A., Bashmal, S., 2007. Vibration analysis of drillstrings with self-excited stick-slip oscillations. J. Sound Vib. 299 (3), 540–558. http://dx.doi.org/10.1016/j.jsv.2006.06.065.

Ladd, A.J., 1994. Numerical simulations of particulate suspensions via a discretized Boltzmann equation. Part 1. Theoretical foundation. J. Fluid Mech. 271, 285–309. http://dx.doi.org/10.1017/S0022112094001771, arXiv:9306004.

Lallemand, P., Luo, L.S., 2000. Theory of the lattice Boltzmann method: Dispersion, dissipation, isotropy, Galilean invariance, and stability. Phys. Rev. E 61 (6), 6546–6562. http://dx.doi.org/10.1103/PhysRevE.61.6546.

Leine, R.I., Van Campen, D.H., Keultjes, W.J., 2002. Stick-slip whirl interaction in drillstring dynamics. J. Vibr. Acoust., Trans. ASME 124 (2), 209–220. http://dx.doi.org/10.1115/1.1452745.

Liu, X., Vlajic, N., Long, X., Meng, G., Balachandran, B., 2014. State-dependent delay influenced drill-string oscillations and stability analysis. J. Vibr. Acoust., Trans. ASME 136 (5), 1–9. http://dx.doi.org/10.1115/1.4027958.

Melakhessou, H., Berlioz, A., Ferraris, G., 2003. A nonlinear well-drillstring interaction model. J. Vibr. Acoust., Trans. ASME 125 (1), 46–52. http://dx.doi.org/10.1115/1.1523071.

Nelson, H.D., McVaugh, J.M., 1976. The dynamics of rotor-bearing systems using finite elements. Trans. ASME, J. Manuf. Sci. Eng. 98 (2), 593–600. http://dx.doi.org/10.1115/1.3438942.

Noble, D.R., Torczynski, J.R., 1998. A lattice-boltzmann method for partially saturated computational cells. Internat. J. Modern Phys. C 9 (8), 1189–1201. http://dx.doi.org/10.1142/S0129183198001084.

Paidoussis, M.P., 1998. Fluid-Structure Interactions: Slender Structures and Axial Flow, Vol. 1. Academic Press.

Peskin, C.S., 1972. Flow patterns around heart valves: a numerical method. J. Comput. Phys. 10 (2), 252–271.

Quemada, D., 1998. Rheological modelling of complex fluids. I. The concept of effective volume fraction revisited. Eur. Phys. J.-Appl. Phys. 1 (1), 119–127.

Rettinger, C., Rüde, U., 2017. A comparative study of fluid-particle coupling methods for fully resolved lattice Boltzmann simulations. Comput. & Fluids 154, 74–89. http://dx.doi.org/10.1016/j.compfluid.2017.05.033, arXiv:1702.04910.

Ritto, T.G., 2010. Numerical Analysis of the Nonlinear Dynamics of a Drill-String with Uncertainty Modeling (Thesis). Pontifícia Universidade Católica do Rio de Janeiro, p. 155.

Tran, Q.T., Nguyen, K.L., Manin, L., Andrianoely, M.A., Dufour, R., Mahjoub, M., Menand, S., 2019. Nonlinear dynamics of directional drilling with fluid and borehole interactions. J. Sound Vib. 462, 114924. http://dx.doi.org/10.1016/j.jsv.2019.114924.

Yigit, A.S., Christoforou, A.P., 2000. Coupled torsional and bending vibrations of actively controlled drillstrings. J. Sound Vib. 234 (1), 67–83. http://dx.doi.org/10.1006/jsvi.1999.2854.

Lucas P. Volpi has a M.Sc degree from the Federal University of Rio de Janeiro in mechanical engineering with an emphasis on vibration and is currently a Ph.D. candidate for petroleum engineering at the University of Stavanger, with focus on fluid dynamics. He is also a researcher on the drilling and well modelling group at the Norwegian Research Centre.

Eric Cayeux is chief scientist for the drilling and well modelling group at the Norwegian Research Centre. He works with multi-disciplinary solutions for well planning, real-time diagnostic of drilling operations, drilling automation, mathematical modelling of the drilling process and sensors. Cayeux holds an M.Sc. degree in civil engineering

from Ecole Nationale des Travaux Publics de l'Etat, Lyon, France, an M.Sc. degree in software engineering from the University of Nice, France, and a Dr. Philos. degree in petroleum engineering from the University of Stavanger, Norway.

Rune W. Time is full professor at the University of Stavanger. He is working mainly with multiphase flow and heat transfer processes, ranging from porous media scale to large scale transport, process and petroleum production. Works are mainly related to experimental fluid dynamics and sensor technology. He has a master (Cand.Real) degree in nuclear high energy physics from University of Bergen and CERN, and a Dr. Scient from University of Bergen in multiphase flow analysis and sensor development.